



## Large contribution of biomass burning emissions to ozone throughout the global remote troposphere

Ilann Bourgeois, Jeff Peischl, J. Andrew Neuman, Steven S Brown, Chelsea R Thompson, Kenneth C Aikin, Hannah M Allen, Hélène Angot, Eric C Apel, Colleen B Baublitz, et al.

### ► To cite this version:

Ilann Bourgeois, Jeff Peischl, J. Andrew Neuman, Steven S Brown, Chelsea R Thompson, et al.. Large contribution of biomass burning emissions to ozone throughout the global remote troposphere. Proceedings of the National Academy of Sciences of the United States of America, 2021, 118 (52), 10.1073/pnas.2109628118 . hal-04382778

**HAL Id: hal-04382778**

**<https://hal.science/hal-04382778>**

Submitted on 9 Jan 2024

**HAL** is a multi-disciplinary open access archive for the deposit and dissemination of scientific research documents, whether they are published or not. The documents may come from teaching and research institutions in France or abroad, or from public or private research centers.

L'archive ouverte pluridisciplinaire **HAL**, est destinée au dépôt et à la diffusion de documents scientifiques de niveau recherche, publiés ou non, émanant des établissements d'enseignement et de recherche français ou étrangers, des laboratoires publics ou privés.



(11, 12), where they are still increasing (13). Additionally, globally averaged tropospheric  $O_3$  has increased over the past five decades (14, 15). Understanding the sources of tropospheric  $O_3$  is thus essential to explain this trend and to inform the development of effective mitigation strategies from regional to hemispheric scales.

Biomass burning (BB) is an important source of  $O_3$  precursors (16–19). A recent study based on observed  $O_3$  to carbon monoxide (CO) enhancements in smoke plumes attributed 3.5% of the global tropospheric chemical  $O_3$  production to BB emissions (19). Other studies have accounted for the numerous production and destruction pathways of  $O_3$  in the troposphere using global chemical transport models (CTMs) to estimate the global budget of  $O_3$  (20, 21). However, few studies separately quantify the contributions of fossil fuel combustion and BB emissions to global tropospheric  $O_3$  (22). Global inventories attribute five times more  $NO_x$  (23, 24) but roughly equal VOC emissions (17, 25) to fossil fuel combustion (hereafter referred to as urban sources) compared with BB. However, precursor emissions do not necessarily determine tropospheric  $O_3$  production close to the sources because of the nonlinearity of  $O_3$  formation chemistry (26, 27). Additionally, global CTMs do not always agree on the tropospheric  $O_3$  burden, suggesting possible deficiencies with emission inventories of  $O_3$  precursors and/or an incomplete representation of  $O_3$  chemistry (21, 28–30), although a recent model intercomparison study showed that the model ensemble reproduced well the salient spatial, seasonal, and decadal variability and trends of tropospheric  $O_3$  (31).

Large-scale in situ observational constraints commensurate with the grid resolution of current global CTMs are rare. Instead, modeling studies often rely on ozonesonde-derived climatologies and satellite-based remote sensing observations to constrain tropospheric  $O_3$  distributions and precursor sources (20, 32, 33). The recent NASA Atmospheric Tomography (ATom) mission provides global-scale and seasonally resolved in situ measurements of  $O_3$  and CO and a comprehensive suite of trace gases and aerosol parameters, including tracers of BB and urban emissions (34). ATom sampled the remote troposphere from the Arctic to the Antarctic over the Pacific and Atlantic Oceans using repeated vertical profiles from ~0.2 to ~13 km in altitude during four seasonal deployments between 2016 and 2018 (Fig. 1). Recently, the ubiquitous presence of dilute BB smoke in the remote troposphere and its significant contribution to aerosol mass loading was established using ATom observations (35). Here, we use ATom measurements to quantify the individual contributions of urban and BB emissions to  $O_3$  in the remote global troposphere using tracers specific to each source. We compare this analysis with simulations from three global CTMs that alternatively set BB and urban emissions to zero to evaluate their impact on modeled tropospheric  $O_3$ .

## Results and Discussion

Here, we analyze in situ measurements of  $O_3$ , ozone precursors, chemical tracers of continental emissions, CO, and water vapor ( $H_2O$ ) to evaluate the influence of urban and BB emissions on  $O_3$  levels in the remote troposphere. We use the industrial solvents tetrachloroethylene ( $C_2Cl_4$ ) and dichloromethane ( $CH_2Cl_2$ ) as tracers of urban and industrial activity, as more than 90% of their global emissions are anthropogenic (36–38). Conversely, we use hydrogen cyanide (HCN) and acetonitrile ( $CH_3CN$ ), compounds emitted almost exclusively (80 to 100%) from BB, as tracers of BB emissions (39–41). All four tracers have an atmospheric lifetime ranging roughly from 2 to 6 mo (40, 42, 43), that is, long enough to identify the influence of emissions on tropospheric  $O_3$ , which has a global average

lifetime of several weeks (28). CO is an atmospheric pollutant released by combustion processes extensively used as a tracer of continental pollution (44) with a global mean atmospheric lifetime of roughly 1 to 3 mo (45, 46). Air masses sampled during ATom were usually within 5 to 10 d downwind of continental pollution sources (47), such that the selected tracers were subject on average to modest (<20%) loss. In this analysis, we combine HCN and  $C_2Cl_4$  as our primary pair of BB and urban tracers and  $CH_3CN$  and  $CH_2Cl_2$  as our secondary pair based on data availability and analytical uncertainty (see details in *SI Appendix, section S1*).

In a previous study, we used the relationship between  $O_3$  and CO during ATom to identify several distinct air mass types: well mixed and aged, stratospheric, marine, and fresh continental outflow (48). Here, we remove data with dominant stratospheric and marine influence as well as the flight segments above the conterminous United States (see Materials and Methods). We thus retain 61% of observations for analysis of the remote troposphere and report the distribution of tropospheric  $O_3$  corresponding to each quartile of  $C_2Cl_4$ ,  $CH_2Cl_2$ , HCN, and  $CH_3CN$  for various regions in *Regionally Enhanced  $O_3$  Levels in Polluted Air Masses*. We separately investigate high  $O_3$  season (spring and summer) and low  $O_3$  season (fall and winter) for both hemispheres. Note that the boreal spring and summer corresponds to the austral fall and winter and vice versa. This seasonal cycle was captured by ATom observations (48) and is typical of tropospheric  $O_3$  globally (49). In *Sources of  $O_3$  to the Remote Troposphere*, we attribute  $O_3$  measured in the remote troposphere to urban and BB sources, and in *Comparison of Observed and Modeled BB Influence on Tropospheric  $O_3$* , we compare our results with global CTMs. All acronyms are listed in *SI Appendix, Table S1*.

### Regionally Enhanced $O_3$ Levels in Polluted Air Masses.

**Northern Hemisphere extratropics (>20°N).** The highest tropospheric  $O_3$  levels were measured in the Northern Hemisphere (Figs. 1 and 2 *A* and *B*) during ATom, with median  $O_3$  mixing ratios of 59 ppbv (parts per billion by volume) in spring and summer and 44 ppbv in fall and winter (median calculated for all altitudes). The Northern Hemisphere also had the largest abundance of CO (*SI Appendix, Fig. S1 A and B*) and urban tracers (*SI Appendix, Fig. S2 A and C*). There was little seasonal difference in the CO abundance, but BB tracer mixing ratios were greater in spring and summer, and urban tracer mixing ratios were greater in fall and winter (*SI Appendix, Fig. S2*).

Greater  $O_3$  levels in spring and summer compared with fall and winter reflect photochemical production of  $O_3$  in both urban- and BB-influenced continental plumes lofted and transported to the remote atmosphere (44, 50–52). While  $O_3$  production is diminished in fall and winter due to reduced sunlight exposure and resulting photochemistry (*SI Appendix, Fig. S3A*),  $O_3$  is still enhanced in polluted air masses relative to the background during those seasons (Fig. 2*B*). Parrish et al. proposed wintertime chemical destruction of  $O_3$  to explain negative  $O_3$  to CO slopes in North American polluted air masses transported over the Atlantic Ocean (53). Here, we find that  $O_3$  does not continuously increase with increasing CO in fall and winter (*SI Appendix, Fig. S4*), but it does continuously increase with increasing urban and BB tracers (Fig. 2*B*). Furthermore, we find that CO continuously increases with increasing levels of urban tracers but not with BB tracers (*SI Appendix, Fig. S1 A and B*). This supports previous findings suggesting that the  $O_3$  to CO correlation can be driven by the mixing of air masses with different origins rather than  $O_3$  production in the remote troposphere (54, 55). The mixing of urban- and BB-influenced air masses affect  $O_3$  and CO levels differently, and the resulting  $O_3$  to CO correlation depends on the composition and age of the mixture.

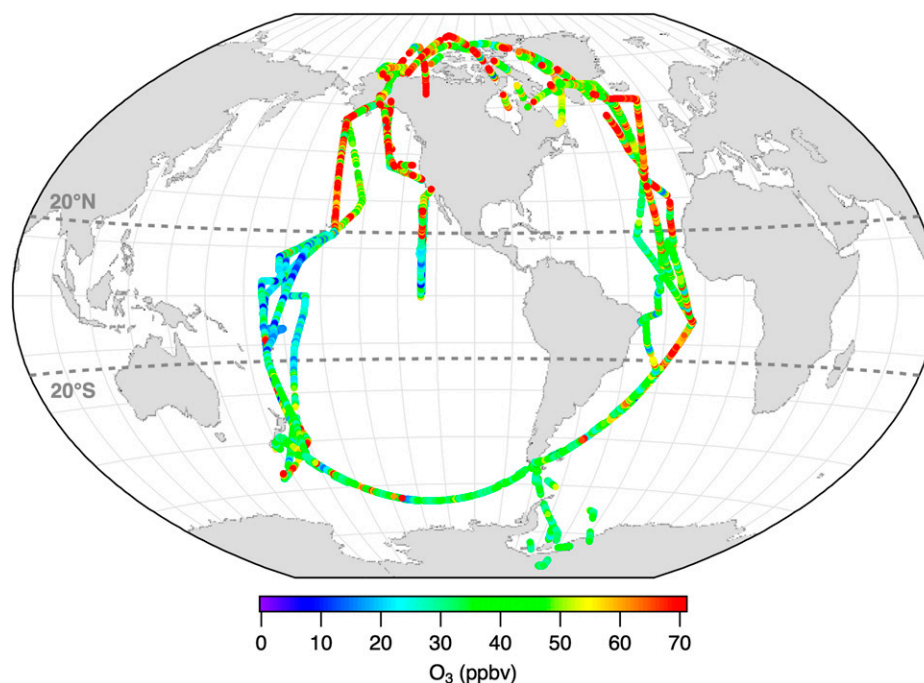


**Fig. 1.** Map of ATom flight tracks from the four seasonal global circuits colored by tropospheric  $O_3$  mixing ratios. Note that the color scale terminates at 70 ppbv of  $O_3$ , and higher values are shown in red. Measurements with a strong stratospheric influence were parsed out as indicated in *Materials and Methods*.

The seasonal and latitudinal differences in background  $O_3$  reveal the contributions of photochemical  $O_3$  production outside of pollution plumes to global tropospheric ozone. Background  $O_3$ , defined as the average  $O_3$  in well-mixed and aged air (air in which both urban and BB tracers are below their regional median), is 15 ppbv greater in spring and summer compared with fall and winter in the Northern Hemisphere (Fig. 2*A* and *B*), a pattern not observed in the Southern Hemisphere (Fig. 2*E* and *F*). Additionally, background  $O_3$  in the Northern Hemisphere spring and summer is 25 ppbv greater than in the Southern Hemisphere spring and summer but only 5 ppbv greater in fall and winter. Attributing this increased and seasonally dependent background  $O_3$  to sources is not possible with our approach.

**Tropics ( $20^\circ S$  to  $20^\circ N$ ).** The tropical Atlantic exhibits the second highest  $O_3$  levels after the Northern Hemisphere extratropics with a median  $O_3$  of 42 ppbv. In contrast, the tropical Pacific has the lowest levels of  $O_3$  with a median  $O_3$  of 25 ppbv despite having a higher abundance of CO (*SI Appendix*, Fig. S1*C*) and urban and BB tracers than the Southern Hemisphere extratropics (*SI Appendix*, Fig. S2).  $O_3$  increased with pollution tracers in both tropical regions (Fig. 2*C* and *D*).

In the tropical Pacific,  $O_3$  (Fig. 2*C*) and CO (*SI Appendix*, Fig. S1*C*) concomitantly increase with increasing urban and BB tracers, suggesting a comparable influence of these emission sources on  $O_3$  in that region (56–58). Low  $O_3$  in the tropical Pacific has been attributed to loss in the marine boundary layer (MBL), where conditions favor the destruction of  $O_3$  via photolysis and subsequent formation of OH at high humidity without concurrent production through the  $HO_x$ - $NO_x$  cycle because of the low  $NO_x$  levels in this region (59–62).

In the tropical Atlantic, the levels of BB tracers are second only to the Northern Hemisphere in spring and summer (*SI Appendix*, Fig. S2*B* and *D*). Additionally,  $O_3$  and CO both increase with increasing levels of BB tracers, a pattern not reproduced with the urban tracers (Fig. 2*D* and *SI Appendix*, Fig. S2*D*), illustrating the overwhelming influence of African

and South American BB emissions on tropospheric  $O_3$  in this region (63–65).

**Southern Hemisphere extratropics ( $>20^\circ S$ ).** The Southern Hemisphere is the most pristine region of those examined here and exhibits the lowest levels of CO (*SI Appendix*, Fig. S1*E* and *F*) and pollution tracers (*SI Appendix*, Fig. S2). Median  $O_3$  mixing ratios were 39 and 34 ppbv in spring and summer and fall and winter, respectively. While little  $O_3$  enhancement above background was observed with increasing pollution tracers in fall and winter (Fig. 2*F*), more active photochemistry in spring and summer (*SI Appendix*, Fig. S3*B*) led to significantly enhanced  $O_3$  above background in polluted air masses (Fig. 2*E*). A more pronounced increase of  $O_3$  (Fig. 2*E* and *F*) and CO (*SI Appendix*, Fig. S1*E* and *F*) with BB tracers than with urban tracers reflect the dominance of BB emissions over urban as a source of pollution in this region inhabited by only ~5% of the world population but with equivalent BB emissions to that in the Northern Hemisphere extratropics (66, 67).

**Sources of  $O_3$  to the Remote Troposphere.** To separately quantify the respective influence of urban and BB emissions on tropospheric  $O_3$ , we classify all sampled air masses into four categories based on observed concentrations of tracers. For each region, polluted air parcels are either defined as urban air (urban tracer > regional median, BB tracer < regional median), BB air (BB tracer > regional median, urban tracer < regional median), or mixed pollution air (both urban and BB tracers > regional median). The remaining data (both urban and BB tracers < regional median) are considered to be well-mixed and aged air. We define the background levels of a given species ( $O_3$ , CO, and the urban and BB tracers) as the average mixing ratio of that species in well-mixed and aged air. This background is regionally and seasonally dependent. Note that this definition of background differs from that used for surface ozone in regulatory applications. For example, air masses with a strong stratospheric influence have been removed in this analysis, but they are usually included in determinations of background ozone used for regulatory purposes. Each category

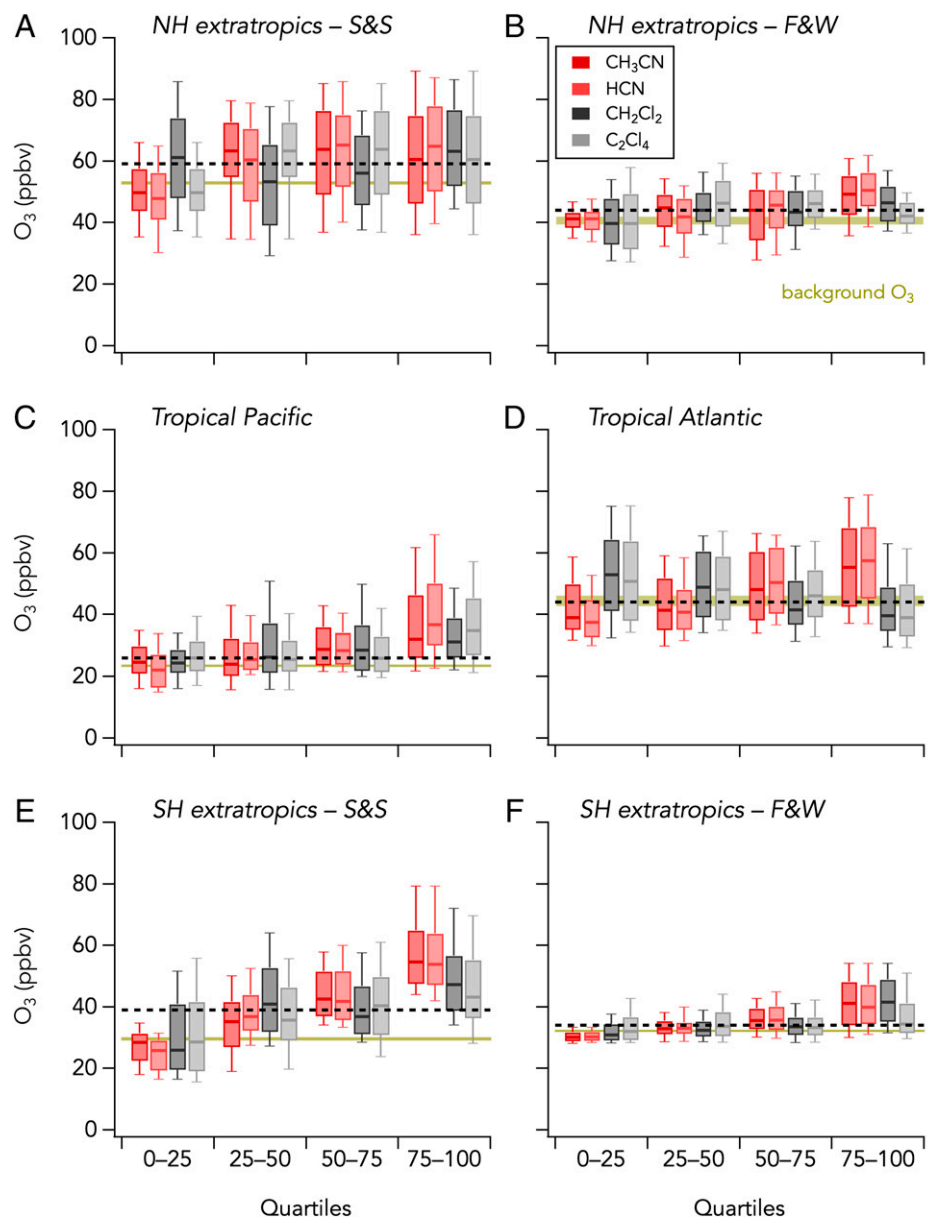


**Fig. 2.** Distributions of tropospheric  $O_3$  mixing ratios (ppbv, y-axis) for each quartile of pollution tracer (x-axis) measured during ATom in four regions of the globe. The colors in the legend indicate the source of the tracers (red for BB, gray for urban). The Northern Hemisphere (NH) extratropics (panels A and B) corresponds to latitudes  $>20^\circ\text{N}$ , the tropics (panels C and D) are defined within  $20^\circ\text{S}$  to  $20^\circ\text{N}$ , and the Southern Hemisphere (SH) extratropics (panels E and F) correspond to latitudes  $>20^\circ\text{S}$ . The NH and SH data are further parsed into a photochemically active period (spring and summer; S&S) and a darker period (fall and winter; F&W). The box and whisker plots show the 10th, 25th, 50th, 75th, and 90th percentiles of  $O_3$  distributions. The mustard-shaded area represents regional background  $O_3$  values defined as the average  $O_3$  mixing ratio in well-mixed and aged air masses. The width of the mustard-shaded area represents the range of background  $O_3$  values obtained when using different pairs of tracers to define the well-mixed and aged air masses. The black dashed lines show regional median  $O_3$  values.

contains roughly equal numbers of observations. The  $O_3$  distribution for each air parcel category is shown in Fig. 3. Excess  $O_3$  (denoted as positive  $\Delta O_3$ ) attributed to each pollution source is the difference between the average  $O_3$  in polluted air (i.e., urban, BB, or mixed pollution) and that in well-mixed and aged air (i.e., regional background  $O_3$ ).

We compare ATom observations with three global CTMs: GEOS-Chem, CAM-chem, and GFDL-AM3 (*SI Appendix, section S2*). Ozone and CO are simulated along the ATom flight tracks in a base case scenario with both anthropogenic and BB emissions (simulation A), zero anthropogenic emissions (simulation B), and zero BB emissions (simulation C). Since CO is directly emitted by both fossil fuel combustion and

BB, anthropogenic CO ( $CO_{UR}$ ) is determined as the difference between simulations A and B, and BB CO ( $CO_{BB}$ ) is determined as the difference between simulations A and C. Using  $CO_{UR}$  as the model urban tracer and  $CO_{BB}$  as the model BB tracer, we derived the modeled  $O_3$  distribution associated with urban, BB, mixed-pollution, and well-mixed and aged air and the corresponding  $\Delta O_3$  following the same methodology as for the observations.

ATom observations show that  $O_3$  levels were generally more enhanced in mixed pollution air, followed by BB air and then urban air, in all regions (Fig. 3). This result is generally consistent for either set of urban and BB tracers used. Larger  $O_3$  levels in mixed pollution air usually reflect increased  $O_3$

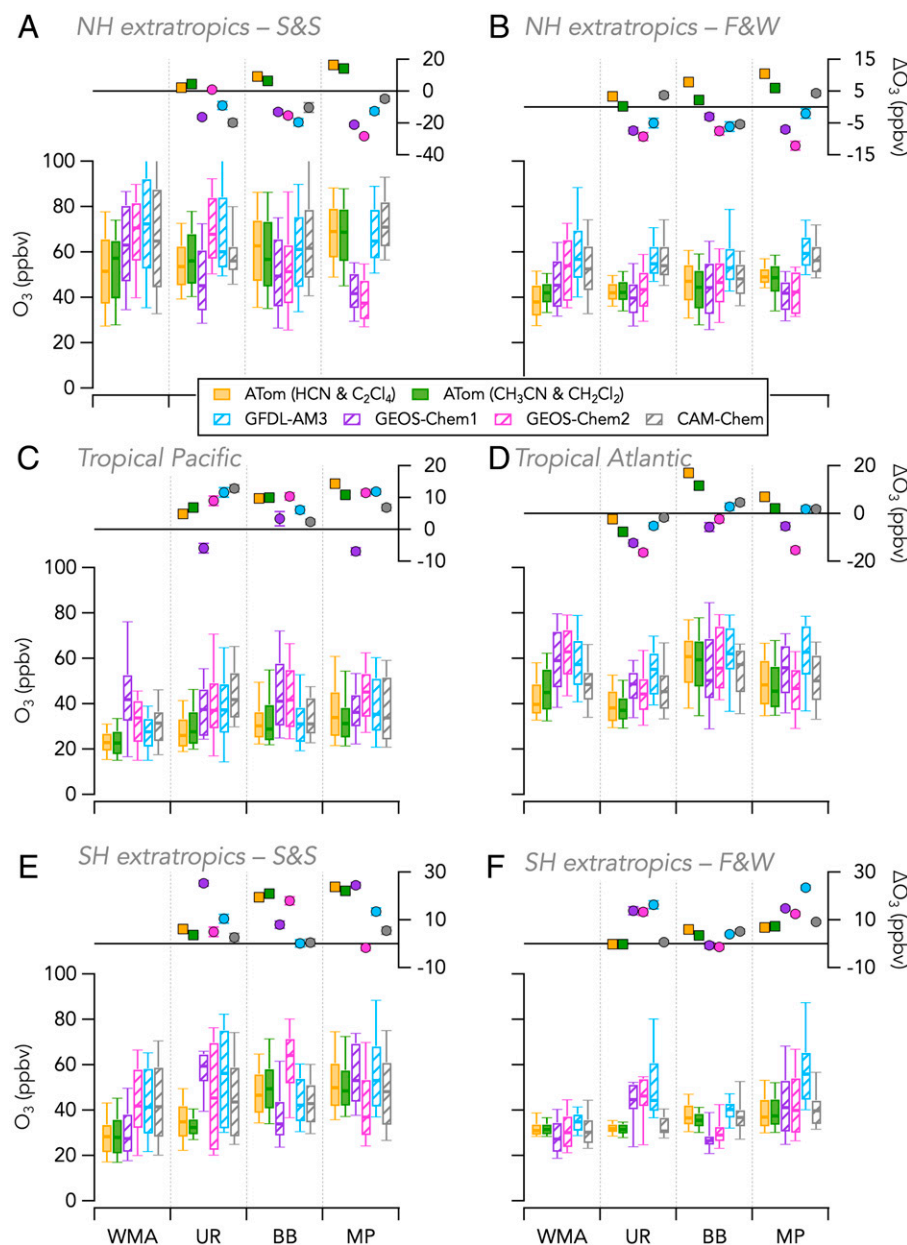


**Fig. 3.** Distributions of tropospheric  $O_3$  (y axis) within each air mass classification (x-axis): well-mixed and aged (WMA) air, urban (UR), BB, or mixed pollution (MP) as defined in *Sources of  $O_3$  to the Remote Troposphere*. The Northern Hemisphere (NH) extratropics (panels A and B), the tropics (panels C and D), and the Southern Hemisphere (SH) extratropics (panels E and F) were defined as in Fig. 2. ATom observations classified using HCN and  $C_2Cl_4$  or  $CH_3CN$  and  $CH_2Cl_2$  pairs of tracers are shown in yellow and green, respectively. Modeling results are shown by the hashed box and whisker plots with GEOS-Chem1 in violet ( $2 \times 2.5^\circ$  horizontal resolution), GEOS-Chem2 in pink ( $4 \times 5^\circ$  horizontal resolution), GFDL-AM3 in light blue, and CAM-chem in gray. The boxes and whiskers show the 10th, 25th, 50th, 75th, and 90th percentiles of  $O_3$  distributions.  $\Delta O_3$  corresponds to the difference between average  $O_3$  in polluted air (i.e., UR, BB, or MP) and that in WMA air.  $\Delta O_3$  is plotted with square markers for ATom observations and round markers for modeling results. The error bars correspond to the SEs of the average  $O_3$  in polluted air and in WMA air added in quadrature.

production (68–70) from greater  $NO_x$  and peroxy acyl nitrates (PANs)—a reservoir species of  $NO_x$ —in mixed-pollution air compared with the BB- or urban-dominated air alone (68–71). We report in Fig. 4 regional median mixing ratios of the four most abundant reactive nitrogen ( $NO_y$ ) species measured during ATom:  $NO_x$ , PANs, and nitric acid ( $HNO_3$ ) as well as particulate nitrate ( $pNO_3$ ).  $NO_y$  concentrations were almost always greatest in mixed-pollution air followed by BB air and then urban air, similar to those for  $O_3$ . The only exception was in the tropical Atlantic, where median  $NO_y$  was highest in BB air, resulting in the highest  $\Delta O_3$  (Fig. 2D). Higher  $NO_y$  concentrations in BB air than in urban air is due to generally higher  $NO_x$

and PANs levels (Fig. 4), a pattern analogous to what is observed for  $O_3$  (Fig. 3). Although global inventories estimate five times more  $NO_x$  emissions from fossil fuel combustion than from BB sources, only a limited fraction of the total  $NO_x$  and PANs emitted in the boundary layer reaches the free troposphere (72, 73). BB emissions, on the other hand, are often convectively injected to higher altitudes, resulting in a proportionally larger amount of BB  $NO_x$  than urban  $NO_x$  injected into the free troposphere (74, 75). In the remote troposphere,  $O_3$  production is driven by the abundance of  $NO_x$  or its reservoir species such as PANs (27, 76, 77). Injection at higher altitude and colder temperatures also increase the lifetime of thermally

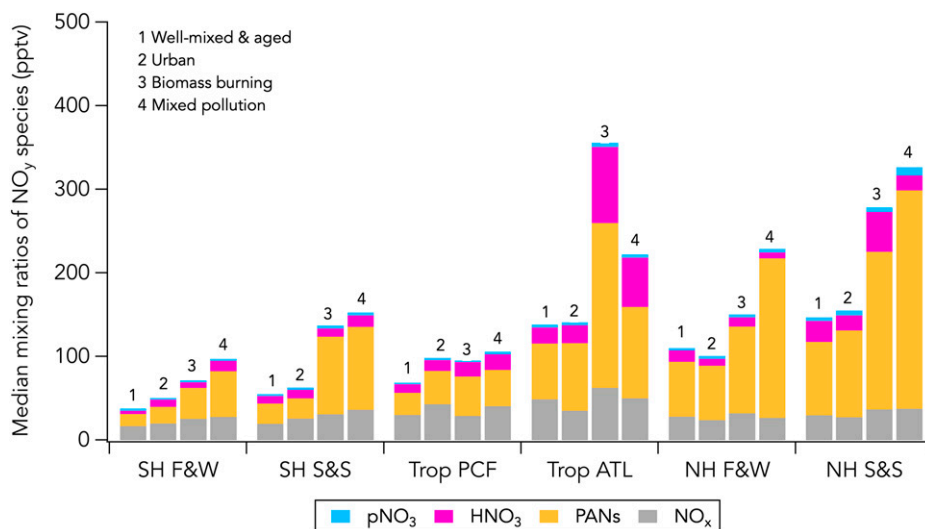


**Fig. 4.** Median mixing ratios of the four main NO<sub>y</sub> species measured during ATom in four air mass types: 1) well mixed and aged, 2) urban, 3) BB, and 4) mixed pollution. NO<sub>y</sub> species are indicated with different colors as shown in the legend.

labile NO<sub>x</sub> reservoirs such as PANs, whose slow thermal decomposition enables sustained ozone production during long-range transport (78).

Often, the global CTMs used here predict lower O<sub>3</sub> in polluted air masses than in well-mixed and aged air, particularly in the Northern Hemisphere and in the tropical Atlantic (negative  $\Delta O_3$ ; Fig. 3 *A*, *B*, and *D*). Greater levels of O<sub>3</sub> in well-mixed and aged air imply that tropospheric O<sub>3</sub> sources in these CTMs are overweighted toward either chemical O<sub>3</sub> production from nonurban and non-BB emissions or stratospheric mixing. Additionally, CTMs often overestimate  $\Delta O_3$  in urban air masses in the Southern Hemisphere in fall and winter and do not reproduce  $\Delta O_3$  in BB and mixed-pollution air masses in the Southern Hemisphere in spring and summer (Fig. 3 *E* and *F*). CTMs sometimes reproduce  $\Delta O_3$  in polluted air masses in the tropical Pacific, where overall O<sub>3</sub> mixing ratios are lowest (Fig. 3 *C*), but they predict significantly [ANOVA test combined with a Tukey post hoc test with a 95% CI (79)] greater levels of O<sub>3</sub> in well-mixed and aged air compared with observations there and in all other regions except for the Southern Hemisphere in fall and winter (Fig. 3). Discrepancies between models and observations highlight gaps in our understanding of tropospheric O<sub>3</sub> sources.

**Comparison of Observed and Modeled BB Influence on Tropospheric O<sub>3</sub>.** To approximately quantify the contributions of BB and urban emissions to O<sub>3</sub>, we first calculate their respective influence on every tropospheric air parcel sampled during ATom in which either the urban or BB tracer was above the regional background value (45 to 76% of the data; *SI Appendix*, Table S2). The fraction of influence is calculated as the ratio of the normalized excess mixing ratio of an urban and BB pollution tracer to CO using ATom observations to its emission ratio from source inventories (see *Materials and Methods*). A simple mixing model shows that variations in the fraction of influence of a source-specific tracer quantitatively represents its mixing with different air mass types (*SI Appendix*, section S4). Next, we calculate the amount of O<sub>3</sub> attributed to urban and BB emissions as the product of the fraction of influence and the amount of O<sub>3</sub> above background. Underlying assumptions and uncertainties are further discussed in *Materials and Methods* and in *SI Appendix*, sections S3–S6. We report the concentration-weighted average O<sub>3</sub> attributed to urban and BB emissions per region in Fig. 5. The concentration-weighted average corresponds to the average regional O<sub>3</sub> attributed to urban/BB emissions weighted

by the urban/BB tracer mixing ratio. Additionally, we estimate the contributions to O<sub>3</sub> from BB and urban emissions using the same simulations from the three global CTMs (Fig. 5). The difference between simulation A (base case) and B (no anthropogenic emissions) is interpreted as urban O<sub>3</sub>, and the difference between simulation A (base case) and C (no BB emissions) is interpreted as BB O<sub>3</sub>.

Observations demonstrate consistently similar or greater O<sub>3</sub> contribution from BB compared with urban emissions in most regions and seasons, with most confidence in the Southern Hemisphere spring and summer and tropical Atlantic. In the Southern Hemisphere and the tropical Atlantic, BB emissions contribute ~2 to 10 times more O<sub>3</sub> than urban emissions. In the Northern Hemisphere and the tropical Pacific, BB and urban emissions contribute similar levels of O<sub>3</sub>. The highest concentration-weighted average O<sub>3</sub> attributed to BB emissions is found in the Southern Hemisphere spring and summer (23.0 to 24.7 ppbv) followed by the tropical Atlantic (10.8 to 12.5 ppbv). The highest concentration-weighted average O<sub>3</sub> attributed to

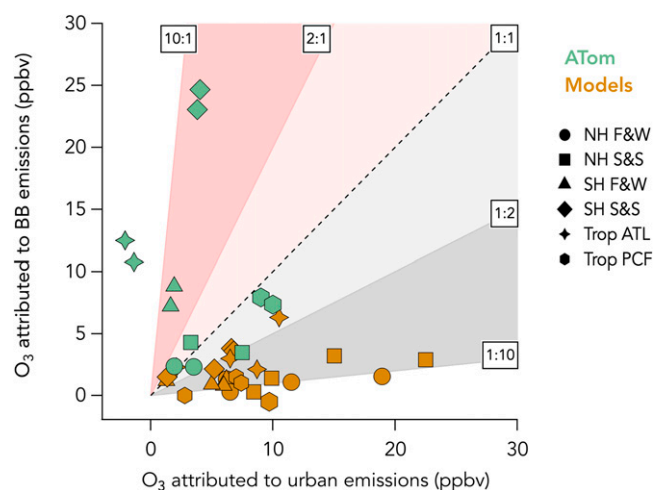


**Fig. 5.** Concentration-weighted average O<sub>3</sub> attributed to urban and BB emissions. ATom observations are shown in green (the two markers per symbol are from the two pairs of tracers used to identify air mass influences), and modeling results are shown in brown. The uncertainties are in *SI Appendix*, Table S3 (observations) and *SI Appendix*, Table S4 (modeling results).

urban emissions is in the tropical Pacific (9.0 to 10.0 ppbv) followed by the Northern Hemisphere spring and summer (3.3 to 7.5 ppbv). The  $O_3$  attribution has a large uncertainty (*SI Appendix, Table S3*), and the methodology applied to derive these numbers is sensitive to many parameters that also have large uncertainties (e.g., background value, emission ratio; *SI Appendix, sections S5 and S6*). However, we apply similar assumptions and parameters to calculate  $O_3$  from urban and BB emissions, which should reduce the uncertainty in the ratio of  $O_3$  attributions to these sources. Consistent results for two sets of urban and BB tracers further support this methodology (Figs. 3 and 5). Additionally, an alternate method consisting of removing air parcels with significant BB or urban influence to evaluate the shift in the regional  $O_3$  distribution also points to a similar or stronger influence from BB than urban emissions on tropospheric  $O_3$  (*SI Appendix, Figs. S6 and S7*). Indeed, removing air masses with large BB or mixed pollution influence generally reduces  $O_3$  by a few ppbv, whereas removing air masses with large urban influence generally shifts the  $O_3$  distribution toward higher values.

None of the models adequately represents the strong influence of BB emissions on tropospheric  $O_3$ . Only one model, GEOS-Chem1, attributed similar  $O_3$  enhancements to BB and urban emissions but only in the Southern Hemisphere and the tropical Atlantic. The other two models, as well as GEOS-Chem1 in the Northern Hemisphere and the tropical Pacific, attribute a factor of 2 to 10 more  $O_3$  to urban than BB emissions. In general, all models ascribe similar or more  $O_3$  to urban emissions than that derived from observations. Since these observation-derived  $O_3$  enhancements are relative to background  $O_3$ , which itself is increased by pollution outflow (80), they are lower estimates of the  $O_3$  contribution from BB and urban emissions. Accounting for contributions from urban and BB emissions to observed background  $O_3$  could reduce the discrepancy with modeled urban  $O_3$  but would likely further increase the gap with modeled BB  $O_3$ .

Discrepancies in the attribution of tropospheric  $O_3$  to BB emissions between observations and model results may arise from a misrepresentation of 1) BB emissions, 2) smoke chemistry, and 3) plume injection height in global models. A correct representation of the injection altitude of smoke in the troposphere is crucial to better predict the impact of BB emissions on the composition of the atmosphere (81). Zhu et al. recently proposed a new global BB emissions injection scheme (not used here by GEOS-Chem), which resulted in significantly better agreement of the simulated vertical profiles of PAN and CO with observations over the North American boreal regions (82). Uncertainty in BB emission inventories has been suggested as a potentially large source of error in global modeling of tropospheric  $O_3$  by the recent Tropospheric Ozone Assessment Report modeling analysis (21). Furthermore, BB emission inventories rely on satellite images of burned areas with coarse spatial resolution and thus significantly underestimate the contribution of undetected small fires (83). Finally,  $O_3$  chemistry in BB plumes is complex and is a topic of intensive current research. Recent findings on the emissions and chemical evolution of  $NO_y$  species (71, 84, 85), VOC emissions (18), and  $O_3$  formation in smoke plumes (86, 87) may improve constraints for global models and enable a better representation of chemical mechanisms in smoke.

**Conclusion and Implications.** Global-scale in situ observations of  $O_3$ , CO, and pollution tracers in the remote troposphere demonstrate that both urban and BB emissions strongly influence global tropospheric  $O_3$ . Air parcels with pollution from both sources exhibit the greatest  $O_3$  enhancements followed by air influenced by BB and then urban emissions in all regions of the globe. A similar pattern is observed for  $NO_y$  species, which

suggests significant  $O_3$  production due to continental pollution in the remote troposphere. All global CTMs used here overpredict  $O_3$  in well-mixed and aged air masses, usually leading to an underprediction of the excess  $O_3$  in polluted air masses when compared with the observations. Observations are analyzed to show that in the Northern Hemisphere, where most urban emissions occur, and in the tropical Pacific,  $O_3$  attributed to BB was within a factor of two of that attributed to urban sources, while in the Southern Hemisphere and in the tropical Atlantic, BB accounted for 2 to 10 times the ozone from urban sources. Conversely, all global CTMs used in this study ascribe a factor of  $\sim 1$  to 10 more  $O_3$  from urban than from BB emissions for the same air parcels, possibly arising from uncertainties in BB emission inventories, chemical mechanisms for  $O_3$  production, plume injection heights, or all three.

On the global scale, anthropogenic activity has increased the tropospheric ozone burden by  $\sim 40\%$  since 1850 (28, 88), with modeled increases at northern midlatitudes of  $\sim 70\%$  since 1850 and  $40\%$  since 1950 (89), in broad agreement with limited observations from the early and mid-20th century (90). In contrast, inventories suggest that global BB emissions have not changed substantially since preindustrialization, as the observed decrease in African emissions since about 1950 has been partially compensated for by an increase in emissions from South America and Asia (66). Nevertheless, there is mounting evidence that BB emissions will play an increasing role in the future composition of the atmosphere due to longer fire seasons (91), more intense fire activity (92), and emissions reductions from fossil fuel combustion. Characterizing these emissions and their impacts at all scales is a subject of intense current public and scientific interest (93–97). Accurate representation of BB emissions and related atmospheric chemistry in global CTMs will be crucial to predicting future levels of tropospheric  $O_3$  and its role in the radiative forcing of climate and air quality. The increased influence of BB  $O_3$  on regional backgrounds compromises the mitigation of  $O_3$  through local emissions reductions to meet air quality standards (98). Estimates of  $O_3$  radiative forcing are dependent on accurate understanding of relevant emission sources and chemistry and may depend more strongly on BB emissions than currently predicted (99). The observational analysis of BB influence at the global scale suggests an incomplete representation of global ozone in current models and points toward several mechanisms requiring further investigation to address these uncertainties.

## Materials and Methods

**Data Parsing.** We used the 2-min merged ATom dataset in this study (34). We removed flight segments over the continental United States to limit the influence of regional emissions. Next, we filtered out marine and stratospheric influences by retaining measurements with  $O_3/H_2O$  between 0.003 and 1 ppbv  $\cdot$  ppmv $^{-1}$  (parts per million by volume). This resulted in 61% of the ATom dataset considered as remote tropospheric air. The thresholds of 0.003 and 1 ppbv  $\cdot$  ppmv $^{-1}$  were chosen based on the inflections in the  $O_3$  to  $O_3/H_2O$  correlation (*SI Appendix, Fig. S7*). A similar filter based on the modeled  $O_3$  and  $H_2O$  was applied to the results from the CTMs. The sensitivity to these filters is further discussed in *SI Appendix, section S3* and illustrated in *SI Appendix, Figs. S9 and S10*. More details about the instrumentation during ATom and the modeling simulations used in this work can be found in *SI Appendix, section S2*.

**Fraction of Influence.** We quantified the respective influence of BB and urban emissions on each air parcel by first calculating the normalized excess mixing ratio (NEMR) of BB and urban tracers according to Eq. 1:

$$NEMR_X = \frac{\Delta X}{\Delta CO} \quad [1]$$

where  $NEMR_X$  is the normalized excess mixing ratio of compound X (i.e.,  $X = HCN, CH_3CN, C_2Cl_4$ , or  $CH_2Cl_2$ ) to CO, and  $\Delta X (\Delta CO)$  is the difference between the mixing ratio of compound X (CO) and its background level. Background levels were defined as the average mixing ratio in well-mixed and aged air

masses, defined as air where both urban and BB tracers are lower than their regional median values (see *Sources of O<sub>3</sub> to the Remote Troposphere*).

The respective influence of urban and BB emissions ( $F_X$ ) was then calculated as the ratio of the NEMR of compound X to the average emission ratio of compound X ( $ER_X$ ) as follows:

$$F_X = \text{NEMR}_X / ER_X \quad [2]$$

The determination of ERs for each pollution tracer is further discussed in *SI Appendix, section S5* and illustrated in *SI Appendix, Fig. S10*. Urban and BB fractions of influence were calculated for air masses with urban or BB tracer levels above their background values, thus limiting the analysis to air parcels with quantifiable continental pollution. The proportion of such air masses is given for each region in *SI Appendix, Table S2*. We present in *SI Appendix, Fig. S11* a histogram of the fractions of influence in the tropical Atlantic as an example. The fractions of influence are distributed around values that reflect the most commonly observed influence from each emission type. In the tropical Atlantic, we show a larger influence of BB compared with urban emissions on polluted air parcels, consistent with our understanding of pollution sources in the area. Further details on the calculation of the fraction of influence are given in *SI Appendix, section S4*.

**O<sub>3</sub> Attribution Calculation.** We attribute tropospheric O<sub>3</sub> above background to urban and BB emissions in polluted air masses as follows:

$$O_3^x = F_X \times \Delta O_3 \quad [3]$$

Then, we calculate the weighted-average O<sub>3</sub> attributed to urban (BB) emissions in each region, which is the average of attributed O<sub>3</sub> in each air parcel weighted by the urban (BB) tracer mixing ratio, as follows:

$$x_{\text{avg}} = \frac{\sum_{i=0}^n w_i \times x_i}{\sum_{i=0}^n w_i} \quad [4]$$

where  $x_{\text{avg}}$  is the weighted-average attributed O<sub>3</sub>,  $x_i$  is the attributed O<sub>3</sub> in the air parcel  $i$ , and  $w_i$  is the weight associated with each value of O<sub>3</sub> attribution equal to the tracer mixing ratio.

One of the assumptions inherent to this O<sub>3</sub> attribution is that O<sub>3</sub> enhancements are linearly correlated with urban and BB tracers. In the remote

troposphere, O<sub>3</sub> production is linearly driven by NO<sub>x</sub> availability (77). However, a significant fraction of tropospheric O<sub>3</sub> may reflect export from the polluted continental boundary layer (73), where O<sub>3</sub> production is nonlinearly determined by the NO<sub>x</sub> to VOCs regime (26). The balance between export from the boundary layer and in situ production of tropospheric O<sub>3</sub> is thus key to assess the validity of this assumption but is not constrained at the global scale. Here, we consider the simultaneous increase of O<sub>3</sub>, CO, and NO<sub>y</sub> species with urban and BB tracers (Figs. 2 and 4 and *SI Appendix, Fig. S1*) as evidence to support a linearity assumption. This simple calculation should thus provide a useful estimate of the average tropospheric O<sub>3</sub> enhancement from each source. We further discuss and illustrate the uncertainty associated with this term in *SI Appendix, section S5, Fig. S12, and Table S3*. A caveat to this methodology is that it assumes similar ozone production efficiency (OPE) from urban and BB emissions. The range of measured  $\Delta O_3$  to  $\Delta CO$ , a proxy of OPE (44), in urban and BB plumes span similar values ( $\sim 0$  to  $1 \text{ ppbv} \cdot \text{ppbv}^{-1}$ ) at the regional scale (19, 63, 100, 101). In our analysis, O<sub>3</sub> detrained from the continental boundary layer to the remote troposphere is integrated over large spatial scales, and the event-scale differences in OPE is likely smoothed out in the process. However, differing OPEs would lead to a corresponding overestimation of the attributed O<sub>3</sub> from the source with the lower OPE.

**Data Availability.** Measurements and modeling work data have been deposited in [https://daac.ornl.gov/ATOM/guides/ATOM\\_merge.html](https://daac.ornl.gov/ATOM/guides/ATOM_merge.html) (<https://doi.org/10.3334/ORNLDAAAC/1581>). Atom and modeling work data used in this study are published through the Distributed Active Archive Center for Biogeochemical Dynamics (34).

**ACKNOWLEDGMENTS.** We thank the ATom leadership team, science team, and DC-8 pilots and crew for contributions to the ATom measurements. ATom was funded in response to NASA ROSES-2013 NRA NNH13ZDA001N-EVS2. We acknowledge support from the US National Oceanic and Atmospheric Administration Atmospheric Chemistry, Carbon Cycle, and Climate (AC4) Program. This material is based upon work supported by the National Center for Atmospheric Research, which is a major facility sponsored by the NSF under Cooperative Agreement No. 1852977. We thank O. Cooper, E. Fischer, P. Wennberg, S. McKeen, and M. Trainer for helpful discussions.

1. P. J. Crutzen, Photochemical reactions initiated by and influencing ozone in unpolluted tropospheric air. *Tellus* **26**, 47–57 (1974).
2. Z. L. Fleming *et al.*, Tropospheric Ozone Assessment Report: Present-day ozone distribution and trends relevant to human health. *Elem. Sci. Anth.* **6**, 12 (2018).
3. G. Mills *et al.*, Tropospheric Ozone Assessment Report: Present-day tropospheric ozone distribution and trends relevant to vegetation. *Elem. Sci. Anth.* **6**, 47 (2018).
4. IPCC, *Climate Change 2013: The Physical Science Basis. Contribution of Working Group I to the Fifth Assessment Report of the Intergovernmental Panel on Climate Change* (Cambridge University Press, Cambridge, UK and New York, NY, 2013).
5. D. Shindell *et al.*, Simultaneously mitigating near-term climate change and improving human health and food security. *Science* **335**, 183–189 (2012).
6. C. E. Junge, Global ozone budget and exchange between stratosphere and troposphere. *Tellus* **14**, 363–377 (1962).
7. H. Simon, A. Reff, B. Wells, J. Xing, N. Frank, Ozone trends across the United States over a period of decreasing NO<sub>x</sub> and VOC emissions. *Environ. Sci. Technol.* **49**, 186–195 (2015).
8. L. Zhang *et al.*, Sources contributing to background surface ozone in the US Intermountain West. *Atmos. Chem. Phys.* **14**, 5295–5309 (2014).
9. D. Kang, R. Mathur, G. A. Pouliot, R. C. Gilliam, D. C. Wong, Significant ground-level ozone attributed to lightning-induced nitrogen oxides during summertime over the Mountain West States. *NPJ Clim. Atmos. Sci.* **3**, 6 (2020).
10. J. J. Guo *et al.*, Average versus high surface ozone levels over the continental USA: Model bias, background influences, and interannual variability. *Atmos. Chem. Phys.* **18**, 12123–12140 (2018).
11. Y. Zhang *et al.*, Tropospheric ozone change from 1980 to 2010 dominated by equatorward redistribution of emissions. *Nat. Geosci.* **9**, 875–879 (2016).
12. Y. Zhang *et al.*, Contributions of world regions to the global tropospheric ozone burden change from 1980 to 2010. *Geophys. Res. Lett.* **48**, e2020GL089184 (2021).
13. R. M. Hoesly *et al.*, Historical (1750–2014) anthropogenic emissions of reactive gases and aerosols from the Community Emissions Data System (CEDS). *Geosci. Model Dev.* **11**, 369–408 (2018).
14. A. Gaudel *et al.*, Aircraft observations since the 1990s reveal increases of tropospheric ozone at multiple locations across the Northern Hemisphere. *Sci. Adv.* **6**, eaba8272 (2020).
15. J. R. Ziemke *et al.*, Trends in global tropospheric ozone inferred from a composite record of TOMS/OMI/MLS/OMP5 satellite measurements and the MERRA-2 GMI simulation. *Atmos. Chem. Phys.* **19**, 3257–3269 (2019).
16. P. J. Crutzen, M. O. Andreae, “Biomass burning in the tropics: Impact on atmospheric chemistry and biogeochemical cycles” in *Paul J. Crutzen: A Pioneer on Atmospheric Chemistry and Climate Change in the Anthropocene*, P. J. Crutzen, H. G. Brauch, Eds. (Springer International Publishing, 2016), pp. 165–188.
17. M. O. Andreae, Emission of trace gases and aerosols from biomass burning – An updated assessment. *Atmos. Chem. Phys.* **19**, 8523–8546 (2019).
18. A. R. Koss *et al.*, Non-methane organic gas emissions from biomass burning: Identification, quantification, and emission factors from PTR-ToF during the FIREX 2016 laboratory experiment. *Atmos. Chem. Phys.* **18**, 3299–3319 (2018).
19. D. A. Jaffe, N. L. Wigder, Ozone production from wildfires: A critical review. *Atmos. Environ.* **51**, 1–10 (2012).
20. L. Hu *et al.*, Global budget of tropospheric ozone: Evaluating recent model advances with satellite (OMI), aircraft (IAGOS), and ozonesonde observations. *Atmos. Environ.* **167**, 323–334 (2017).
21. P. J. Young *et al.*, Tropospheric Ozone Assessment Report: Assessment of global-scale model performance for global and regional ozone distributions, variability, and trends. *Elem. Sci. Anth.* **6**, 10 (2018).
22. J. Mao *et al.*, Sensitivity of tropospheric oxidants to biomass burning emissions: Implications for radiative forcing. *Geophys. Res. Lett.* **40**, 1241–1246 (2013).
23. T. Stavrou *et al.*, Key chemical NO<sub>x</sub> sink uncertainties and how they influence top-down emissions of nitrogen oxides. *Atmos. Chem. Phys.* **13**, 9057–9082 (2013).
24. C. Wiedinmyer *et al.*, The Fire INventory from NCAR (FINN): A high resolution global model to estimate the emissions from open burning. *Geosci. Model Dev.* **4**, 625–641 (2011).
25. Intergovernmental Panel on Climate Change, “Clouds and aerosols” in *Climate Change 2013 – The Physical Science Basis: Working Group I Contribution to the Fifth Assessment Report of the Intergovernmental Panel on Climate Change* (Cambridge University Press, 2014), pp. 571–658.
26. X. Lin, M. Trainer, S. C. Liu, On the nonlinearity of the tropospheric ozone production. *J. Geophys. Res. Atmos.* **93**, 15879–15888 (1988).
27. S. C. Liu *et al.*, Ozone production in the rural troposphere and the implications for regional and global ozone distributions. *J. Geophys. Res. Atmos.* **92**, 4191–4207 (1987).
28. P. J. Young *et al.*, Pre-industrial to end 21st century projections of tropospheric ozone from the Atmospheric Chemistry and Climate Model Intercomparison Project (ACCMIP). *Atmos. Chem. Phys.* **13**, 2063–2090 (2013).
29. W. Shiliang *et al.*, Why are there large differences between models in global budgets of tropospheric ozone? *J. Geophys. Res. Atmos.* **112**, D05302 (2007).
30. R. G. Derwent *et al.*, Uncertainties in models of tropospheric ozone based on Monte Carlo analysis: Tropospheric ozone burdens, atmospheric lifetimes and surface distributions. *Atmos. Environ.* **180**, 93–102 (2018).

31. P. T. Griffiths *et al.*, Tropospheric ozone in CMIP6 simulations. *Atmos. Chem. Phys.* **21**, 4187–4218 (2021).
32. J. R. Ziemke *et al.*, Tropospheric ozone determined from Aura OMI and MLS: Evaluation of measurements and comparison with the Global Modeling Initiative's Chemical Transport Model. *J. Geophys. Res. Atmos.* **111**, D19303 (2006).
33. S. Tilmes *et al.*, Technical Note: Ozone-sonde climatology between 1995 and 2011: Description, evaluation and applications. *Atmos. Chem. Phys.* **12**, 7475–7497 (2012).
34. S. C. Wofsy *et al.*, ATom: Merged Atmospheric Chemistry, Trace Gases, and Aerosols. ORNL DAAC (2018). <https://doi.org/10.3334/ORNLDAAC/1581> (Accessed 2 October, 2020).
35. G. P. Schill *et al.*, Widespread biomass burning smoke throughout the remote troposphere. *Nat. Geosci.* **13**, 422–427 (2020).
36. P. G. Simmonds *et al.*, Global trends, seasonal cycles, and European emissions of dichloromethane, trichloroethene, and tetrachloroethene from the AGAGE observations at Mace Head, Ireland, and Cape Grim, Tasmania. *J. Geophys. Res. Atmos.* **111**, D18304 (2006).
37. S. A. Montzka *et al.*, "Scientific assessment of ozone depletion" in *Ozone-Depleting Substances (ODSs) and Related Chemicals*. (World Meteorological Organization, Geneva, Switzerland, 2011), pp. 1–112.
38. T. Claxton *et al.*, A synthesis inversion to constrain global emissions of two very short lived chlorocarbons: Dichloromethane and perchloroethylene. *J. Geophys. Res. Atmos.* **125**, e2019JD031818 (2020).
39. R. Holzinger *et al.*, Biomass burning as a source of formaldehyde, acetaldehyde, methanol, acetone, acetonitrile, and hydrogen cyanide. *Geophys. Res. Lett.* **26**, 1161–1164 (1999).
40. M. Le Breton *et al.*, Airborne hydrogen cyanide measurements using a chemical ionisation mass spectrometer for the plume identification of biomass burning forest fires. *Atmos. Chem. Phys.* **13**, 9217–9232 (2013).
41. J. A. de Gouw *et al.*, Emission sources and ocean uptake of acetonitrile ( $\text{CH}_3\text{CN}$ ) in the atmosphere. *J. Geophys. Res. Atmos.* **108**, 4329 (2003).
42. R. Hossaini *et al.*, Recent trends in stratospheric chlorine from very short-lived substances. *J. Geophys. Res. Atmos.* **124**, 2318–2335 (2019).
43. H. B. Singh *et al.*, In situ measurements of HCN and  $\text{CH}_3\text{CN}$  over the Pacific Ocean: Sources, sinks, and budgets. *J. Geophys. Res. Atmos.* **108**, 8795 (2003).
44. D. D. Parrish *et al.*, Export of North American ozone pollution to the North Atlantic Ocean. *Science* **259**, 1436–1439 (1993).
45. M. J. Prather, Lifetimes and time scales in atmospheric chemistry. *Philos. Trans.-Royal Soc., Math. Phys. Eng. Sci.* **365**, 1705–1726 (2007).
46. D. Ehhalt *et al.*, "Atmospheric chemistry and greenhouse gases" in *IPCC Third Assessment Report Climate Change 2001: The Scientific Basis* (Cambridge University Press, Cambridge, United Kingdom, 2001), 238–289.
47. X. Chen *et al.*, HCOOH in the remote atmosphere: Constraints from Atmospheric Tomography (ATom) airborne observations. *ACS Earth Space Chem.* **5**, 1436–1454 (2021).
48. I. Bourgeois *et al.*, Global-scale distribution of ozone in the remote troposphere from the ATom and HIPPO airborne field missions. *Atmos. Chem. Phys.* **20**, 10611–10635 (2020).
49. A. Gaudel *et al.*, Tropospheric Ozone Assessment Report: Present-day distribution and trends of tropospheric ozone relevant to climate and global atmospheric chemistry model evaluation. *Elem. Sci. Anth.* **6**, 39 (2018).
50. M. Parrington *et al.*, The influence of boreal biomass burning emissions on the distribution of tropospheric ozone over North America and the North Atlantic during 2010. *Atmos. Chem. Phys.* **12**, 2077–2098 (2012).
51. R. E. Newell, M. J. Evans, Seasonal changes in pollutant transport to the North Pacific: The relative importance of Asian and European sources. *Geophys. Res. Lett.* **27**, 2509–2512 (2000).
52. J. A. Logan, Tropospheric ozone: Seasonal behavior, trends, and anthropogenic influence. *J. Geophys. Res. Atmos.* **90**, 10463–10482 (1985).
53. D. D. Parrish, T. B. Ryerson, J. S. Holloway, M. Trainer, F. C. Fehsenfeld, New directions: Does pollution increase or decrease tropospheric ozone in Winter–Spring? *Atmos. Environ.* **33**, 5147–5149 (1999).
54. O. R. Cooper, J. L. Moody, T. D. Thornberry, M. S. Town, M. A. Carroll, PROPHET 1998 meteorological overview and air-mass classification. *J. Geophys. Res. Atmos.* **106**, 24289–24299 (2001).
55. J. A. Neuman *et al.*, Relationship between photochemical ozone production and  $\text{NO}_x$  oxidation in Houston, Texas. *J. Geophys. Res.* **114**, D00F08 (2009).
56. M. G. Schultz *et al.*, On the origin of tropospheric ozone and  $\text{NO}_x$  over the tropical South Pacific. *J. Geophys. Res. Atmos.* **104**, 5829–5843 (1999).
57. S. J. Oltmans *et al.*, Ozone in the Pacific tropical troposphere from ozonesonde observations. *J. Geophys. Res. Atmos.* **106**, 32503–32525 (2001).
58. B. D. Martin *et al.*, Long-range transport of Asian outflow to the equatorial Pacific. *J. Geophys. Res. Atmos.* **107**, 8322 (2002).
59. D. Kley *et al.*, Observations of near-zero ozone concentrations over the convective Pacific: Effects on air chemistry. *Science* **274**, 230–233 (1996).
60. D. D. Parrish *et al.*, Seasonal cycles of  $\text{O}_3$  in the marine boundary layer: Observation and model simulation comparisons. *J. Geophys. Res. Atmos.* **121**, 538–557 (2016).
61. A. M. Thompson *et al.*, Ozone observations and a model of marine boundary layer photochemistry during SAGA 3. *J. Geophys. Res. Atmos.* **98**, 16955–16968 (1993).
62. H. B. Singh *et al.*, Reactive nitrogen and ozone over the western Pacific: Distribution, partitioning, and sources. *J. Geophys. Res. Atmos.* **101**, 1793–1808 (1996).
63. D. L. Mauzerall *et al.*, Photochemistry in biomass burning plumes and implications for tropospheric ozone over the tropical South Atlantic. *J. Geophys. Res. Atmos.* **103**, 8401–8423 (1998).
64. L. Jourdain *et al.*, Tropospheric vertical distribution of tropical Atlantic ozone observed by TES during the northern African biomass burning season. *Geophys. Res. Lett.* **34**, L04810 (2007).
65. M. O. Andreae *et al.*, Influence of plumes from biomass burning on atmospheric chemistry over the equatorial and tropical South Atlantic during CITE 3. *J. Geophys. Res.* **99**, 12793 (1994).
66. M. J. E. van Marle *et al.*, Historic global biomass burning emissions for CMIP6 (BB4CMIP) based on merging satellite observations with proxies and fire models (1750–2015). *Geosci. Model Dev.* **10**, 3329–3357 (2017).
67. M. Kumm, O. Varis, The world by latitudes: A global analysis of human population, development level and environment across the north–south axis over the past half century. *Appl. Geogr.* **31**, 495–507 (2011).
68. C. E. Buysse, A. Kaulfus, U. Nair, D. A. Jaffe, Relationships between particulate matter, ozone, and nitrogen oxides during urban smoke events in the western US. *Environ. Sci. Technol.* **53**, 12519–12528 (2019).
69. C. D. McClure, D. A. Jaffe, Investigation of high ozone events due to wildfire smoke in an urban area. *Atmos. Environ.* **194**, 146–157 (2018).
70. J. Lindaas *et al.*, Changes in ozone and precursors during two aged wildfire smoke events in the Colorado Front Range in summer 2015. *Atmos. Chem. Phys.* **17**, 10691–10707 (2017).
71. J. F. J. Calahorrano *et al.*, Daytime oxidized reactive nitrogen partitioning in western U.S. wildfire smoke plumes. *J. Geophys. Res. Atmos.* **126**, e2020JD033484 (2020).
72. D. J. Jacob *et al.*, Factors regulating ozone over the United States and its export to the global atmosphere. *J. Geophys. Res. Atmos.* **98**, 14817–14826 (1993).
73. Q. Li, D. J. Jacob, J. W. Munger, R. M. Yantosca, D. D. Parrish, Export of  $\text{NO}_x$  from the North American boundary layer: Reconciling aircraft observations and global model budgets. *J. Geophys. Res. Atmos.* **109**, D02313 (2004).
74. H. Huntrieser *et al.*, Injection of lightning-produced  $\text{NO}_x$ , water vapor, wildfire emissions, and stratospheric air to the UT/LS as observed from DC3 measurements. *J. Geophys. Res. Atmos.* **121**, 6638–6668 (2016).
75. M. Val Martin, R. A. Kahn, M. G. Tosca, A global analysis of wildfire smoke injection heights derived from space-based multi-angle imaging. *Remote Sens.* **10**, 1609 (2018).
76. J. L. Laughner, R. C. Cohen, Direct observation of changing  $\text{NO}_x$  lifetime in North American cities. *Science* **366**, 723–727 (2019).
77. W. L. Chameides *et al.*, Ozone precursor relationships in the ambient atmosphere. *J. Geophys. Res. Atmos.* **97**, 6037–6055 (1992).
78. R. C. Hudman *et al.*, Ozone production in transpacific Asian pollution plumes and implications for ozone air quality in California. *J. Geophys. Res. Atmos.* **109**, D23S10 (2004).
79. W. C. Driscoll, Robustness of the ANOVA and Tukey–Kramer statistical tests. *Comput. Ind. Eng.* **31**, 265–268 (1996).
80. D. A. Jaff *et al.*, Scientific assessment of background ozone over the U.S.: Implications for air quality management. *Elementa (Wash D C)* **6**, 56 (2018).
81. R. Paugam, M. Wooster, S. Freitas, M. Val Martin, A review of approaches to estimate wildfire plume injection height within large-scale atmospheric chemical transport models. *Atmos. Chem. Phys.* **16**, 907–925 (2016).
82. L. Zhu *et al.*, Development and implementation of a new biomass burning emissions injection height scheme (BBEIH v1.0) for the GEOS-Chem model (v9-01-01). *Geosci. Model Dev.* **11**, 4103–4116 (2018).
83. R. Ramo *et al.*, African burned area and fire carbon emissions are strongly impacted by small fires undetected by coarse resolution satellite data. *Proc. Natl. Acad. Sci. U.S.A.* **118**, e2011160118 (2021).
84. J. Lindaas *et al.*, Emissions of reactive nitrogen from western U.S. wildfires during Summer 2018. *J. Geophys. Res. Atmos.* **125**, e2020JD032657 (2020).
85. Q. Peng *et al.*, HONO emissions from Western U.S. wildfires provide dominant radical source in fresh wildfire smoke. *Environ. Sci. Technol.* **54**, 5954–5963 (2020).
86. M. M. Coggon *et al.*, OH chemistry of non-methane organic gases (NMOGs) emitted from laboratory and ambient biomass burning smoke: Evaluating the influence of furans and oxygenated aromatics on ozone and secondary NMOG formation. *Atmos. Chem. Phys.* **19**, 14875–14899 (2019).
87. M. A. Robinson *et al.*, Variability and time of day dependence of ozone photochemistry in western wildfire plumes. *Environ. Sci. Technol.* **55**, 10280–10290 (2021).
88. L. Y. Yeung *et al.*, Isotopic constraint on the twentieth-century increase in tropospheric ozone. *Nature* **570**, 224–227 (2019).
89. R. B. Skeie *et al.*, Historical total ozone radiative forcing derived from CMIP6 simulations. *NPJ Clim. Atmos. Sci.* **3**, 32 (2020).
90. D. W. Tarasick *et al.*, Tropospheric Ozone Assessment Report: Tropospheric ozone from 1877 to 2016, observed levels, trends and uncertainties. *Elem. Sci. Anth.* **7**, 39 (2019).
91. W. M. Jolly *et al.*, Climate-induced variations in global wildfire danger from 1979 to 2013. *Nat. Commun.* **6**, 7537 (2015).
92. D. M. J. S. Bowman *et al.*, Human exposure and sensitivity to globally extreme wildfire events. *Nat. Ecol. Evol.* **1**, 58 (2017).
93. B. Zheng *et al.*, Increasing forest fire emissions despite the decline in global burned area. *Sci. Adv.* **7**, eab2646 (2021).
94. M. Burke *et al.*, The changing risk and burden of wildfire in the United States. *Proc. Natl. Acad. Sci. U.S.A.* **118**, e2011048118 (2021).

95. F. H. Johnston *et al.*, Unprecedented health costs of smoke-related PM<sub>2.5</sub> from the 2019–20 Australian megafires. *Nat. Sustain.* **4**, 42–47 (2021).
96. I. R. van der Velde *et al.*, Vast CO<sub>2</sub> release from Australian fires in 2019–2020 constrained by satellite. *Nature* **597**, 366–369 (2021).
97. D. A. Jaffe *et al.*, Wildfire and prescribed burning impacts on air quality in the United States. *J. Air Waste Manag. Assoc.* **70**, 583–615 (2020).
98. O. R. Cooper, A. O. Langford, D. D. Parrish, D. W. Fahey, Atmosphere. Challenges of a lowered U.S. ozone standard. *Science* **348**, 1096–1097 (2015).
99. D. Shindell *et al.*, Role of tropospheric ozone increases in 20th-century climate change. *J. Geophys. Res. Atmos.* **111**, D08302 (2006).
100. Y. Kondo *et al.*, Impacts of biomass burning in Southeast Asia on ozone and reactive nitrogen over the western Pacific in spring. *J. Geophys. Res. Atmos.* **109**, D15S12 (2004).
101. R. E. Honrath *et al.*, Regional and hemispheric impacts of anthropogenic and biomass burning emissions on summertime CO and O<sub>3</sub> in the North Atlantic lower free troposphere. *J. Geophys. Res. Atmos.* **109**, D24310 (2004).